Infrared Absorption by Ferroelectric Thin Film Structures Utilizing Novel Conducting Oxides

R. C. Hoffman, W. A. Beck, C. W. Tipton, D. N. Robertson, M. Z. Tidrow, W. W. Clark
Army Research Laboratory
Adelphi, MD
K. R. Udayakumar, H. R. Beratan, Kevin Soch, and C. M. Hanson
Raytheon Systems
Dallas, TX

ABSTRACT

Infrared absorbing air-bridge structures are anticipated to be used in the next generation of ferroelectric uncooled infrared detectors. These structures will consist of resonant cavities with an absorbing bridge element, which contains the ferroelectric detector and the contact electrodes. An oxide electrode is preferable to a metallic electrode, because the metallic electrode reflects too much of the incoming radiation at reasonable thickness. For this paper, spectral transmission and reflection of lanthanum nickelate (LNO), barium ruthenate (BRO) and strontium ruthenate (SRO) films were measured, and it was found that the properties could be described as a simple two-dimensional conducting sheet. The optical absorption of several air-bridge structures was modeled, and optimized dimensions and electrode conductivity are presented which yield greater than 80% absorption over the full 8-14 μm band.

INTRODUCTION

Uncooled infrared focal plane arrays composed of thin-film ferroelectric (FE) detecting elements show great promise for low-cost infrared imaging with projected temperature sensitivity below 10 mK with *f*/1 optics. To achieve high optical absorption with low thermal mass, air-bridge structures will be used in which optical resonance between the FE layer and the underlying read-out integrated circuit (ROIC) is used to enhance absorption over the 8 to 14 μm long wavelength infrared (LWIR) spectral band.

As shown in Figure 1(a), the simplest resonant absorption structure consists of a conducting film with sheet resistivity equal to the free-space impedance $Z_0 = 120\pi\ \Omega$, spaced one-fourth of a wavelength ($\lambda/4$) above the reflecting surface. Such a structure has a theoretical absorption of 100 percent at the design wavelength. The desired detector/ROIC is more like the structure shown in Figure 1(b). It includes a finite-thickness FE element with conducting electrodes on both sides suspended over the ROIC.

Form SF298 Citation Data

Report Date ("DD MON YYYY") 00001999	Report Type N/A	Dates Covered (from... to) ("DD MON YYYY")

Title and Subtitle Infrared Absorption by Ferroelectric Thin Film Structures Utilizing Novel Conducting Oxides	**Contract or Grant Number**
	Program Element Number
Authors	**Project Number**
	Task Number
	Work Unit Number
Performing Organization Name(s) and Address(es) Army Research Laboratory Adelphi, MD	**Performing Organization Number(s)**
Sponsoring/Monitoring Agency Name(s) and Address(es)	**Monitoring Agency Acronym**
	Monitoring Agency Report Number(s)
Distribution/Availability Statement Approved for public release, distribution unlimited	
Supplementary Notes	
Abstract	
Subject Terms	
Document Classification unclassified	**Classification of SF298** unclassified
Classification of Abstract unclassified	**Limitation of Abstract** unlimited
Number of Pages 19	

Early versions of the thin-film FE pixel structure at Raytheon have used a 3000-Å-thick FE layer with a thick opaque platinum electrode and a semitransparent NiCr front electrode. This pixel structure was used to maximize process yield in early devices, although, as shown later, the optical absorption is lower than will be achieved in structures with semitransparent front and back electrodes.

In this paper, we measure the optical transmission and reflection of promising semitransparent electrode materials lanthanum nickelate (LNO), barium ruthenate (BRO) and strontium ruthenate (SRO. We determine optimum values for the electrode conductivity and FE-ROIC cavity spacing to maximize the absorption of the actual detector structure at a specified wavelength and computed the absorption spectrum over the LWIR band.

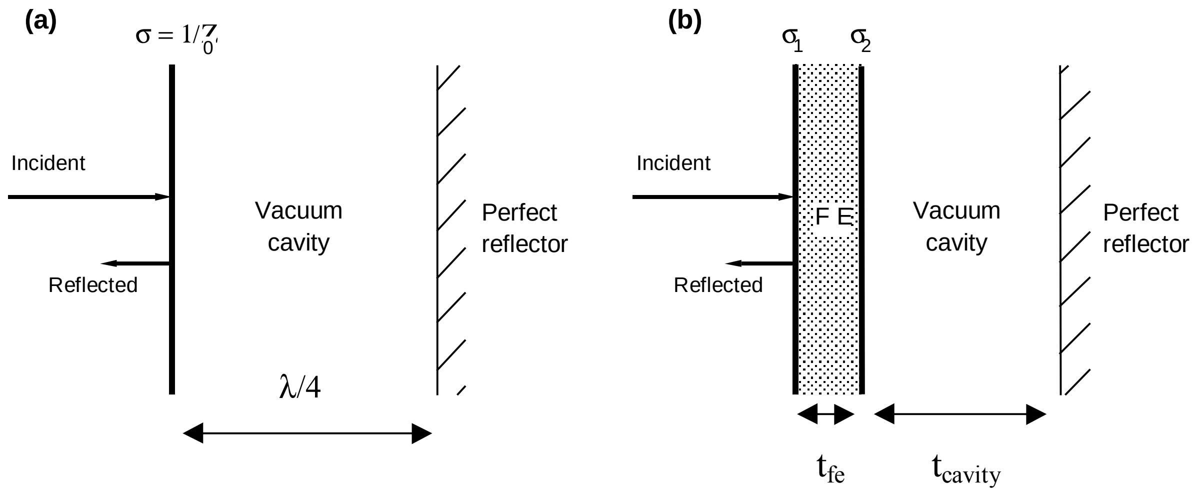

Figure 1: Optical absorption structures: (a) Simple $\lambda/4$ structure and (b) actual detector structure with ferroelectric (FE) layer, electrodes (σ_1 and σ_2), and vacuum cavity over perfectly reflecting ROIC.

EXPERIMENTAL

The LNO, BRO and SRO films were deposited on two-side polished Si substrates with the use of a RF sputtering deposition system from stoichiometric targets. The substrate temperature was maintained at 25 ºC during the deposition. All depositions were performed in an Ar environment at 7 mTorr. Spectroscopic observations showed that under these conditions no oxidation of the Si substrate occurred. Following deposition, the films were heated in either an oven at 500 ºC for 10 min, or a rapid thermal annealer (RTA) at temperatures ranging from 400 ºC to 550 ºC for 60 sec.

The LNO set included thicknesses of 1620, 1240, 740, and 450Å. The films were either oven-annealed for 10 min at 500°C or rapid thermal annealed for 60 sec at nominal temperatures of 550 °C or 600 °C. The BRO set included thicknesses of 1561, 907, 545, and 317Å. The films were rapid thermal annealed (RTA) for 60 sec at nominal temperatures of 400, 450, 500 or 550 °C. The SRO set included thicknesses of 2000Å, 1000Å, and 500Å. The films were heated in the RTA for 60 sec at nominal temperatures of 400, 450, 500 or 550 °C.

The reflection from (and therefore absorption in) the structure was computed using a 2 x 2 transfer matrix formulation.[1] The FE layer was assumed to have an isotropic refractive index of n = 2.24 and no absorption for most calculations. The effect of varying n between 2.1 and 2.5[2] was also determined for some results. The surface of the ROIC was assumed to be a perfectly reflecting mirror. The electrodes were approximated as thin (two-dimensional) sheets with specified sheet conductivity.

RESULTS AND DISCUSSION

LNO Results

Figure 2 shows the measured transmittance and reflectance for the films that were oven-annealed at 500°C for 10 min. To interpret these measurements, we computed the expected transmission and reflection for a two-dimensional conducting layer on a Si substrate as a function of the layer conductivity.[3] Because no interference fringes from the Si substrate were observed, presumably due to small thickness variations, we assumed that reflections from the two Si surfaces were incoherent.

Figure 3 shows the analytical result, along with the measured values extracted from the data in Figure 2. Figure 4 shows the σZ_0 and sheet σ implied in Figure 3 versus the LNO thickness. The sheet conductivity increases approximately linearly with film thickness, corresponding to a bulk resistivity of 0.25 mΩ-cm. Figure 5 shows the analytical result of films heat treated in the RTA for 60 sec at 550 ºC. Figure 6 shows the σZ_0 and sheet σ implied by Figure 5 versus the LNO thickness. The sheet conductivity increases approximately linearly with film thickness, corresponding to a bulk resistivity of 0.52 mΩ-cm. Figure 7 shows the analytical result, along with the measured values extracted from the optical data for films rapid thermal annealed at 600°C for 60sec. Figure 8 shows the σZ_0 and sheet σ implied by Figure 7 versus the LNO thickness. The sheet conductivity increases approximately linearly with film thickness, corresponding to a bulk resistivity of 0.56 mΩ-cm.

Table 1 shows a summary of the LNO results. The conductivities of the oven-annealed LNO films were all much higher than the optimum value for detector coupling. Even the thinnest film (450 Å) had an implied sheet conductivity of greater than 5 / Z_0 compared to the optimum value of ~0.5 / Z_0 (for equal-conductivity electrodes). A shorter or lower temperature anneal is required for proper optical coupling.

The conductivities of the RTA films was about half that of the oven-annealed films. Surprisingly, there was only a small difference between the RTA films annealed at 550°C and those annealed at 600°C. The conductivities still appear much higher than the optimum value. The thinnest film (450 A) had an implied sheet conductivity of ~2.5 / Z_0 compared to the optimum value of ~0.5 / Z_0.

Table 1: Summary of results.

Anneal	Bulk resistivity (mΩ-cm)	σ / Z_0 for 450 Å film
Oven at 500°C for 10 min	0.25	5.2
RTA at 550°C for 60 sec	0.52	2.5
RTA at 600°C for 60 sec	0.56	2.4

BRO Results

Figures 9 to 12 again show the analytical result, along with the measured values extracted from the optical data. The sheet conductance of the films is generally lower than the desired value of ~0.5/ Z_0, except for the thickest film. Because the sheet conductances were so low, no attempt was made to plot the values versus thickness.

SRO Results

Figures 13 to 16 again show the analytical result, along with the measured values extracted from the optical data. The sheet conductance of these films covers the desired range quite well at the lower anneal temperatures. For example, with the 400 °C anneal the 500 and 1000 Å films appear to be close to the desired sheet conductance. Figure 17 shows the σZ_0 and sheet σ implied by Figures 13 to 16 versus the SRO thickness. Note that the sheet conductance is not proportional to film thickness, i.e., there is an extrapolated finite sheet conductance at zero film thickness. This effect could be associated with an actual surface conductance on the SRO, but is more likely caused by surface roughness that scatters light and thereby shifts the points in Figures 13 to 16 to lower transmission and apparently higher conductance. The bulk resistivities implied by the slopes of the linear fits are indicated the figure.

(a)

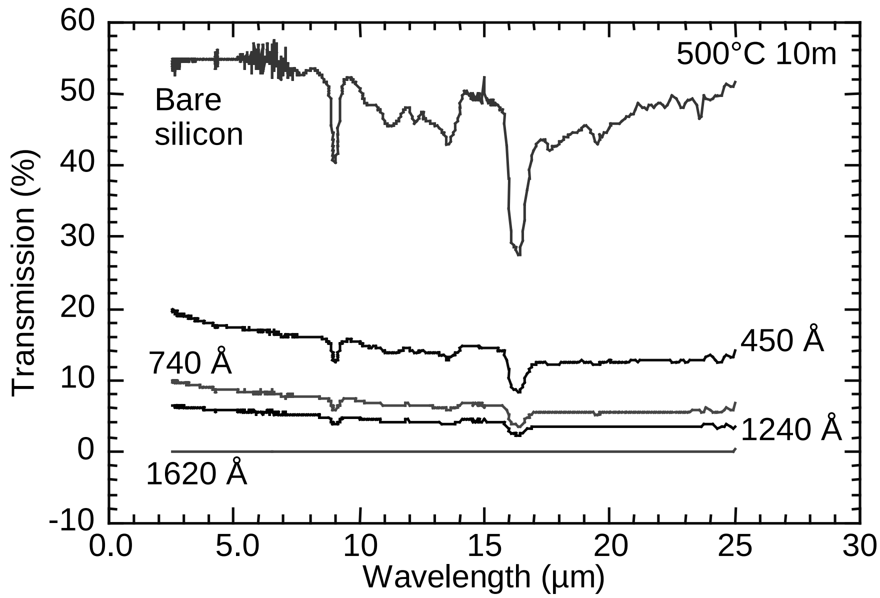

(b)

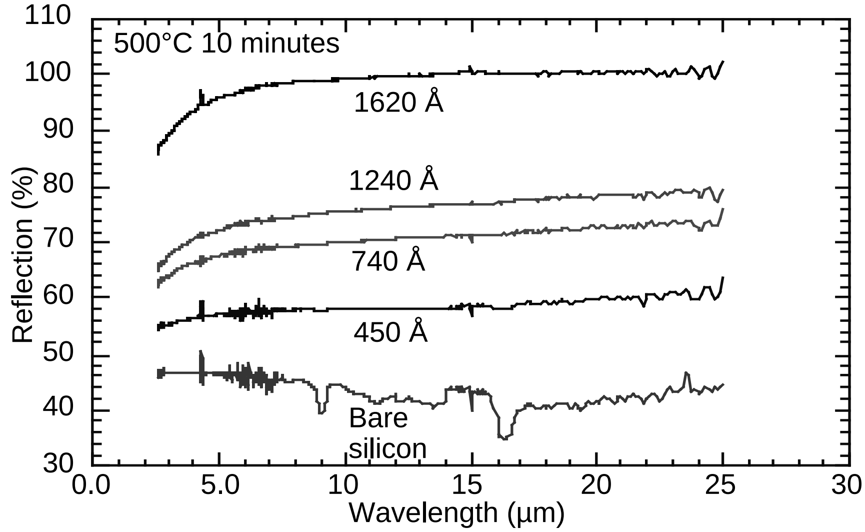

Figure 2: (a) Transmission and (b) reflection for LNO layers on Si substrate (oven annealed at 500°C for 10 min). LNO thickness is indicated.

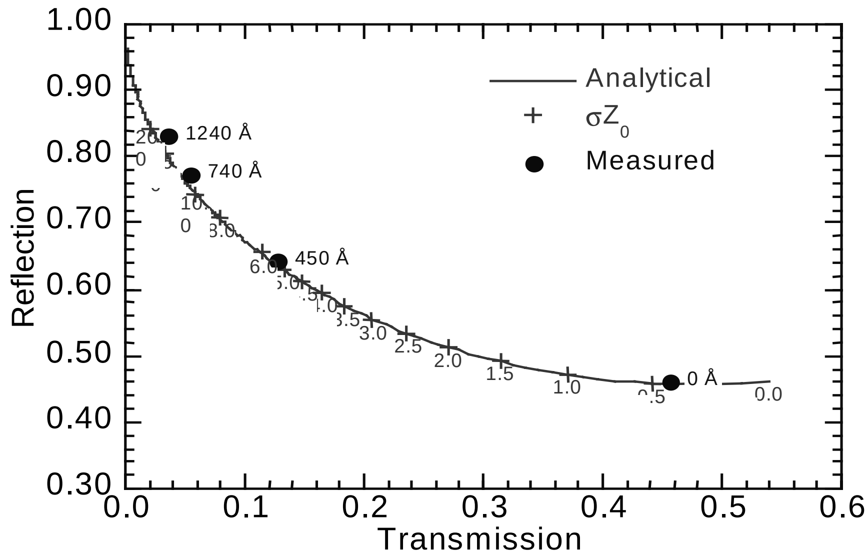

Figure 3: Reflection vs. transmission for two-dimensional conducting layer of LNO on Si substrate (oven annealed at 500 °C for 10 min). Solid line is analytical result, bullets are from measured data in Figure 2, and crosses indicate σZ_0 corresponding to analytical result.

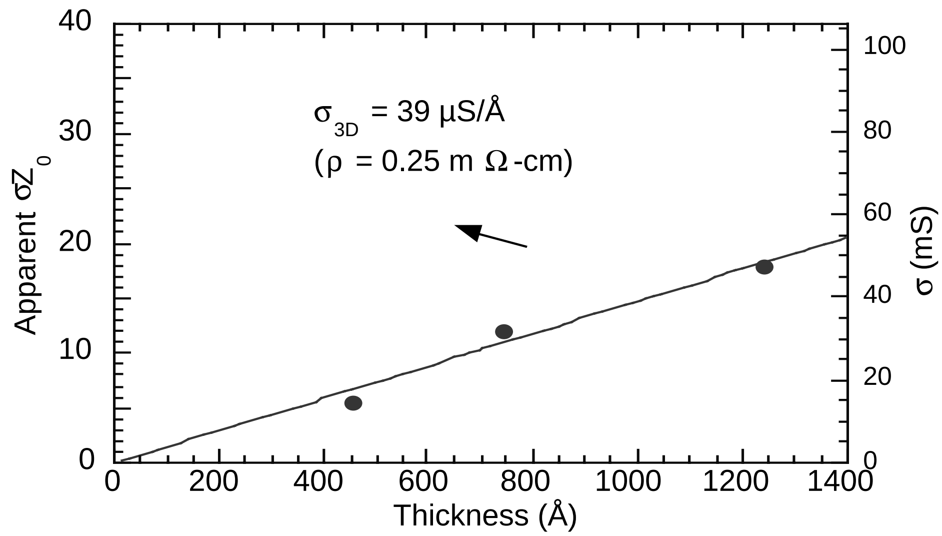

Figure 4: Apparent value of σZ_o (left axis) and corresponding sheet conductivity (right axis) from Figure 3 vs. LNO thickness (oven annealed at 500 °C for 10 min). Solid line is linear fit indicating bulk conductivity and resistivity.

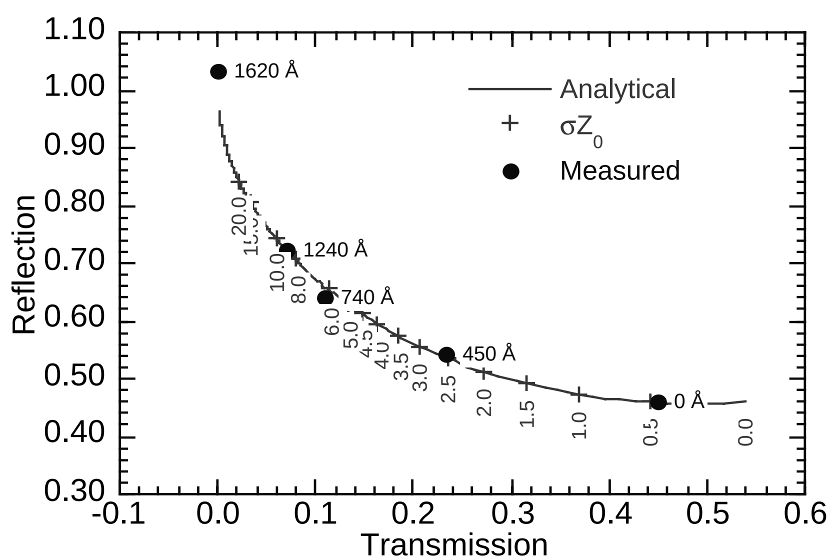

Figure 5: Reflection vs. transmission for two-dimensional conducting layer of LNO on Si substrate (RTA at 550 °C for 60 sec). Solid line is analytical result, bullets are from measured data in Figure 2, and crosses indicate σZ_0 corresponding to analytical result.

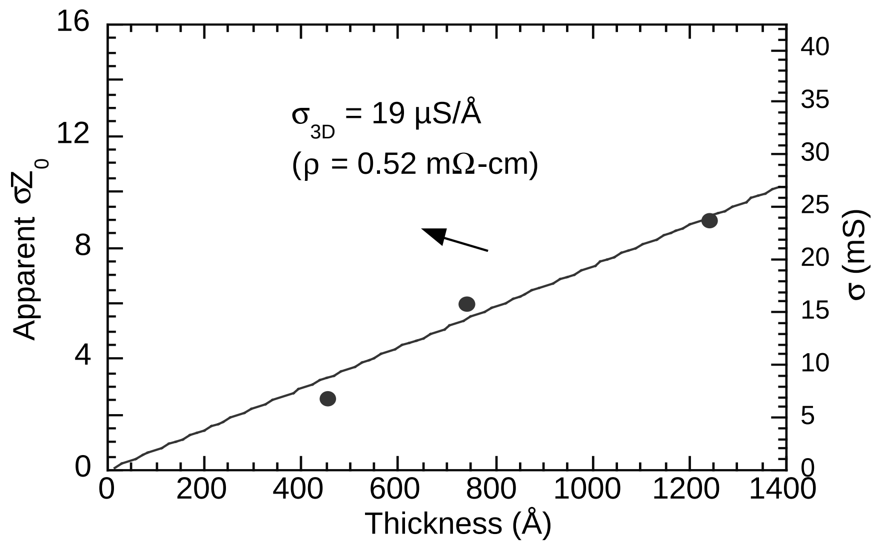

Figure 6: Apparent value of σZ_0 (left axis) and corresponding sheet conductivity (right axis) from Figure 5 vs. LNO thickness (RTA at 550°C for 60 sec). Solid line is linear fit indicating bulk conductivity and resistivity.

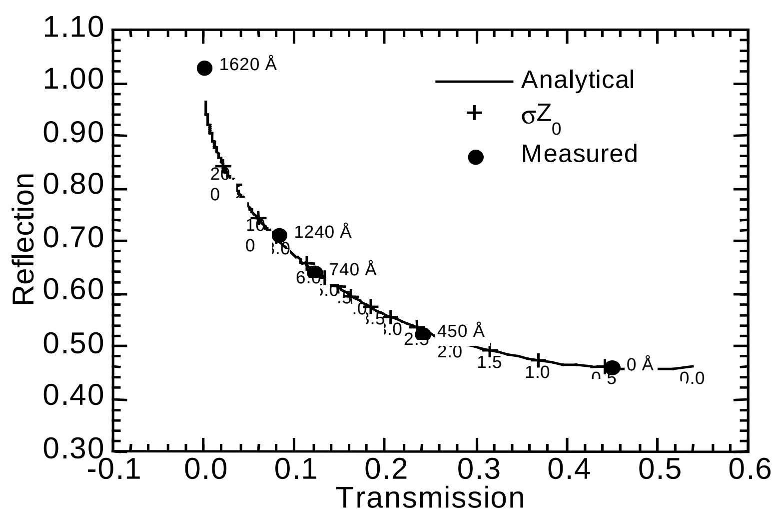

Figure 7: Reflection vs. transmission for two-dimensional conducting layer on Si substrate (RTA at 600 °C for 60 sec). Solid line is analytical result, bullets are from measured LNO data, and crosses indicate σZ_0 corresponding to analytical result.

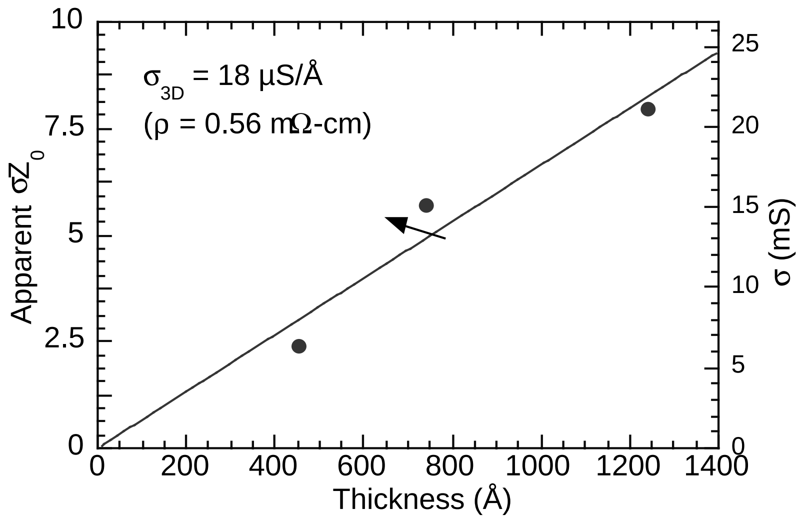

Figure 8: Apparent value of σZ_0 (left axis) and corresponding sheet conductivity (right axis) from Figure 7- vs. LNO thickness (RTA at 600 °C for 60 sec). Solid line is linear fit indicating bulk conductivity and resistivity.

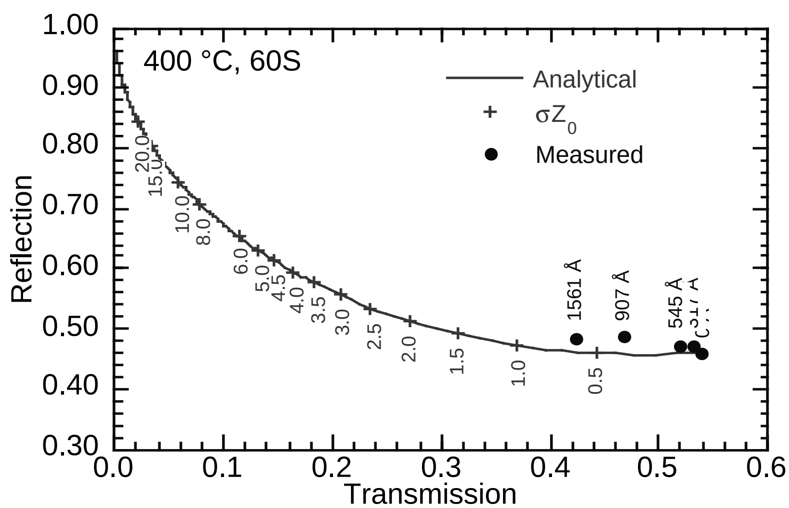

Figure 9: Reflection vs. transmission for two-dimensional conducting layer on Si substrate (400 °C for 60 sec). Solid line is analytical result, bullets are from measured BRO data, and crosses indicate σZ_0 corresponding to analytical result.

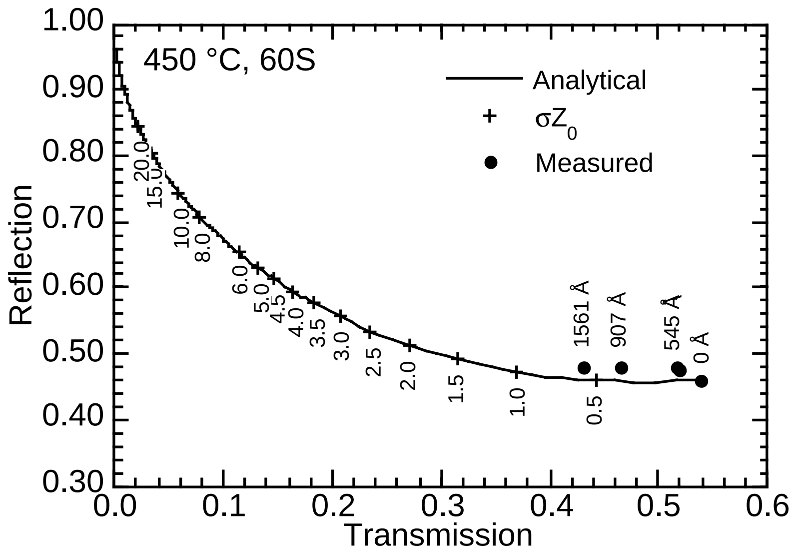

Figure 10: Reflection vs. transmission for two-dimensional conducting layer on Si substrate (450 °C for 60 sec). Solid line is analytical result, bullets are from measured BRO data, and crosses indicate σZ_0 corresponding to analytical result.

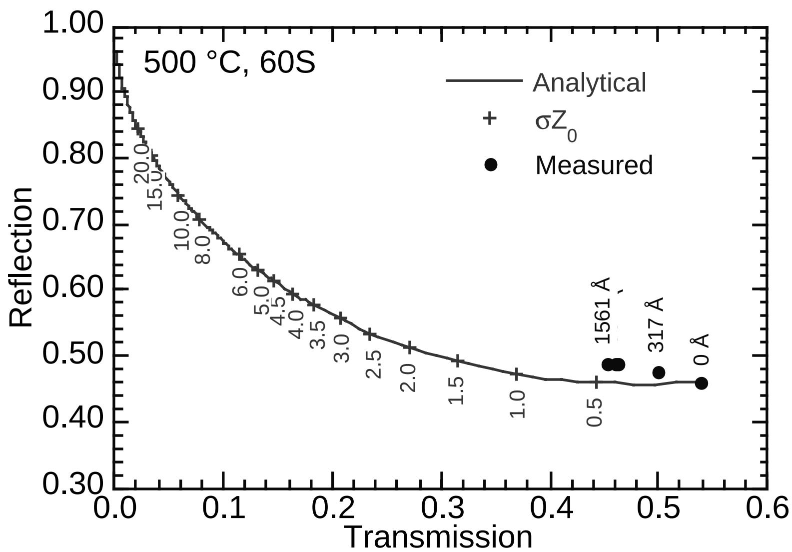

Figure 11: Reflection vs. transmission for two-dimensional conducting layer on Si substrate (500 °C for 60 sec). Solid line is analytical result, bullets are from measured BRO data, and crosses indicate σZ_0 corresponding to analytical result.

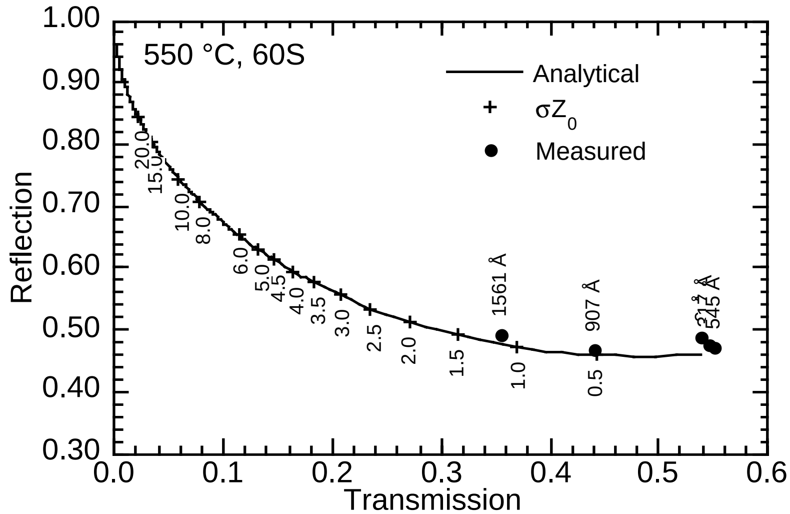

Figure 12: Reflection vs. transmission for two-dimensional conducting layer on Si substrate (550 °C for 60 sec). Solid line is analytical result, bullets are from measured BRO data, and crosses indicate σZ_0 corresponding to analytical result.

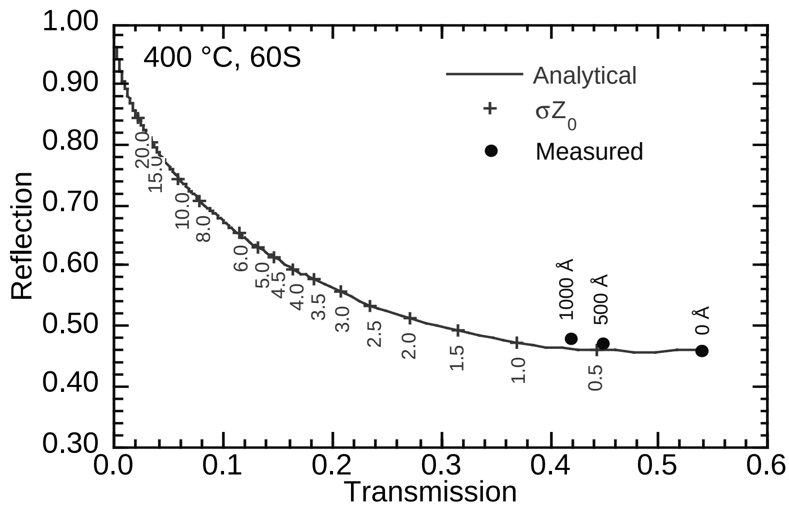

Figure 13: Reflection vs. transmission for two-dimensional conducting layer on Si substrate (400 °C for 60 sec). Solid line is analytical result, bullets are from measured SRO data, and crosses indicate σZ_0 corresponding to analytical result. Apparently anomalous data at 2000 Å thickness is not shown.

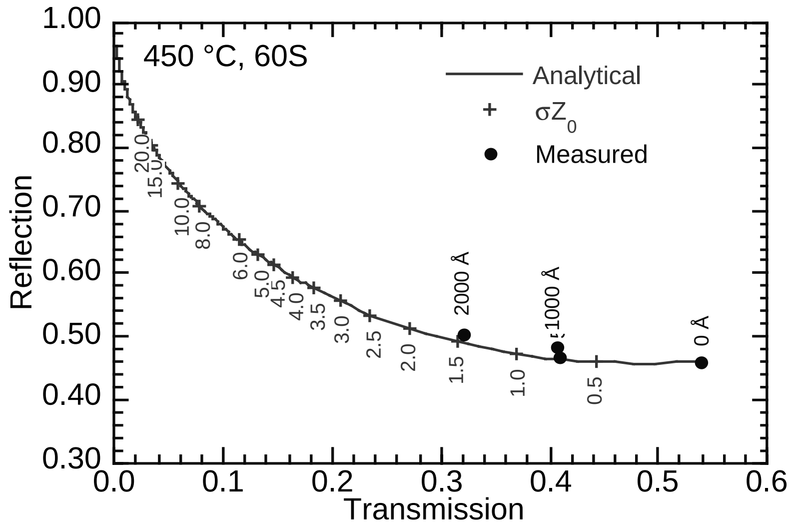

Figure 14: Reflection vs. transmission for two-dimensional conducting layer on Si substrate (450 °C for 60 sec). Solid line is analytical result, bullets are from measured SRO data, and crosses indicate σZ_0 corresponding to analytical result.

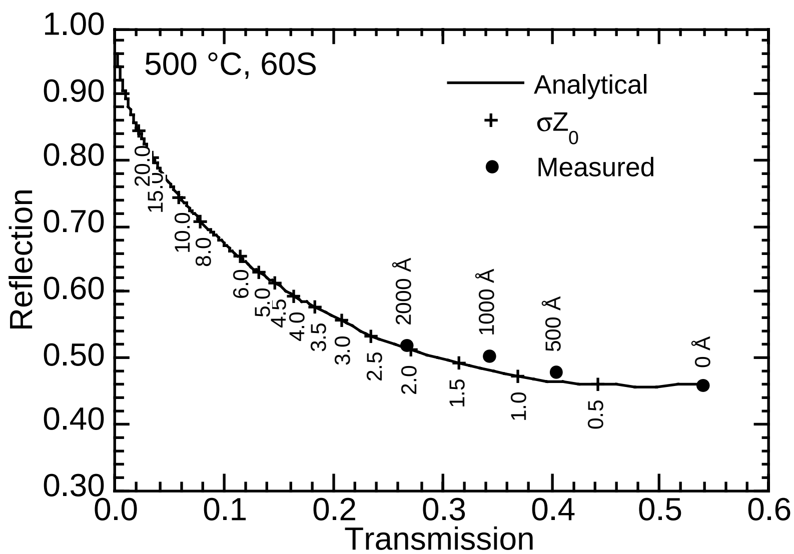

Figure 15: Reflection vs. transmission for two-dimensional conducting layer on Si substrate (500 °C for 60 sec). Solid line is analytical result, bullets are from measured SRO data, and crosses indicate σZ_0 corresponding to analytical result.

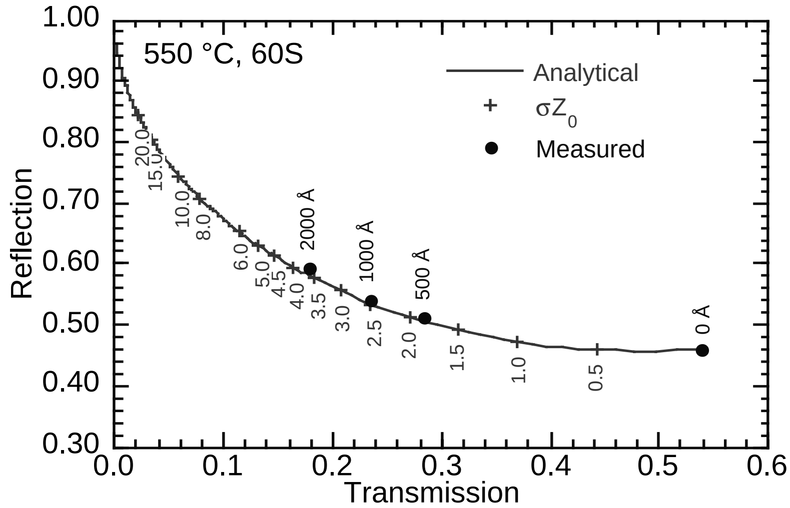

Figure 16: Reflection vs. transmission for two-dimensional conducting layer on Si substrate (550 °C for 60 sec). Solid line is analytical result, bullets are from measured SRO data, and crosses indicate σZ_0 corresponding to analytical result.

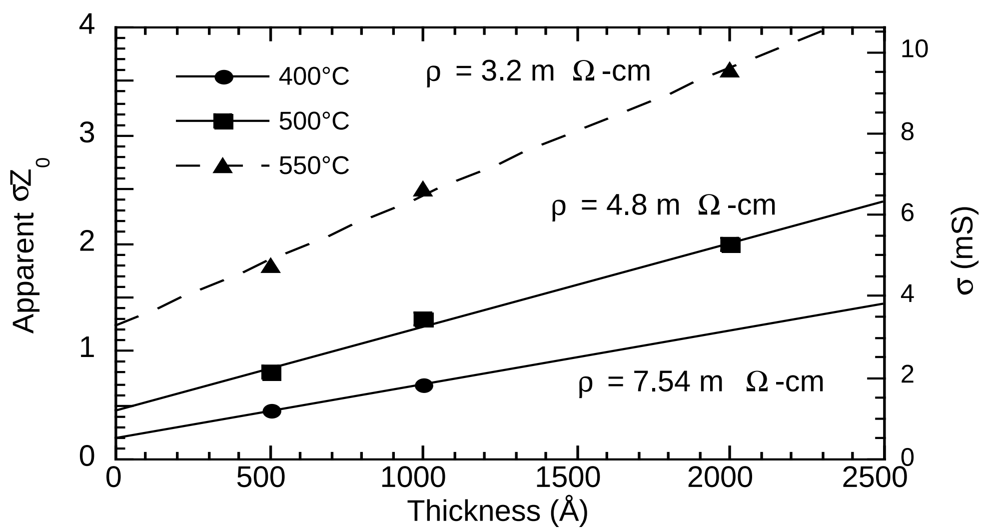

Figure 17: Apparent value of σZ_o (left axis) and corresponding sheet conductivity (right axis) vs. SRO thickness (anneal temperature indicated). The fact that the linear fits do not pass through the origin implies some surface effect. Bulk resistivities implied by the *slopes* of the curves are indicated.

DETECTOR MODELING – $\lambda/4$ STRUCTURE

For comparison to other results, the absorption spectrum of a simple $\lambda/4$ structure (Figure 1(a)) that was optimized for a wavelength of 11 µm is shown in Figure 18. Note that the absorption is greater than 90 percent over the full LWIR band.

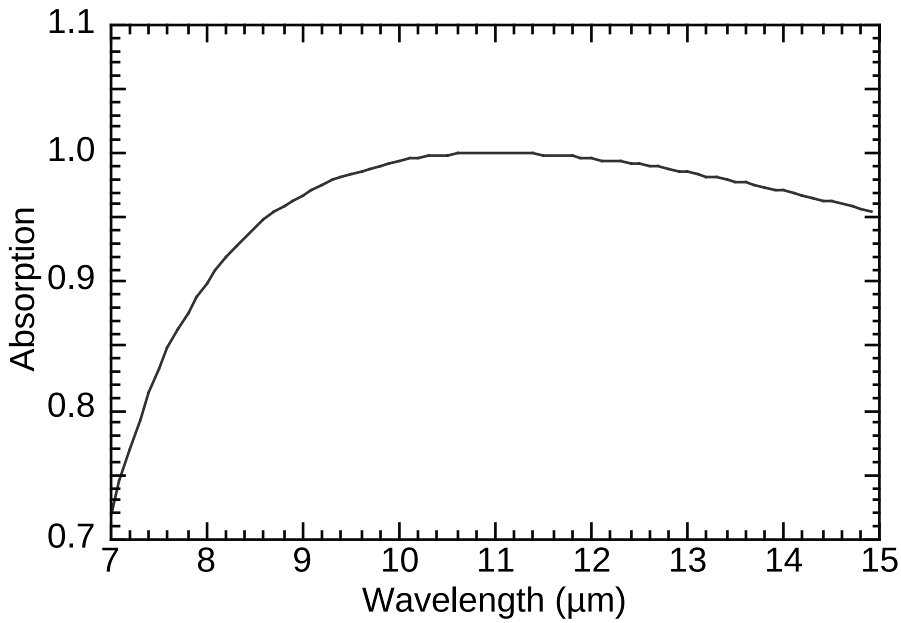

Figure 18: Absorption spectrum for simple $\lambda/4$ cavity structure optimized for λ = 11 µm.

Semitransparent Front Electrode with Opaque Back Electrode

As mentioned previously, early devices use an opaque back electrode and semi-transparent front electrode on a 3000 Å FE layer. Figure 19 shows the computed absorption spectra for the structure. The spectra were computed for a front-electrode conductivity of $1/Z_0$, and also for a more optimized front-electrode conductivity of $5.5/Z_0$. The FE layer is too thin to form an optimum cavity; therefore the absorption is limited to 20 to 40 percent over the LWIR band, even with optimized electrode conductivity.

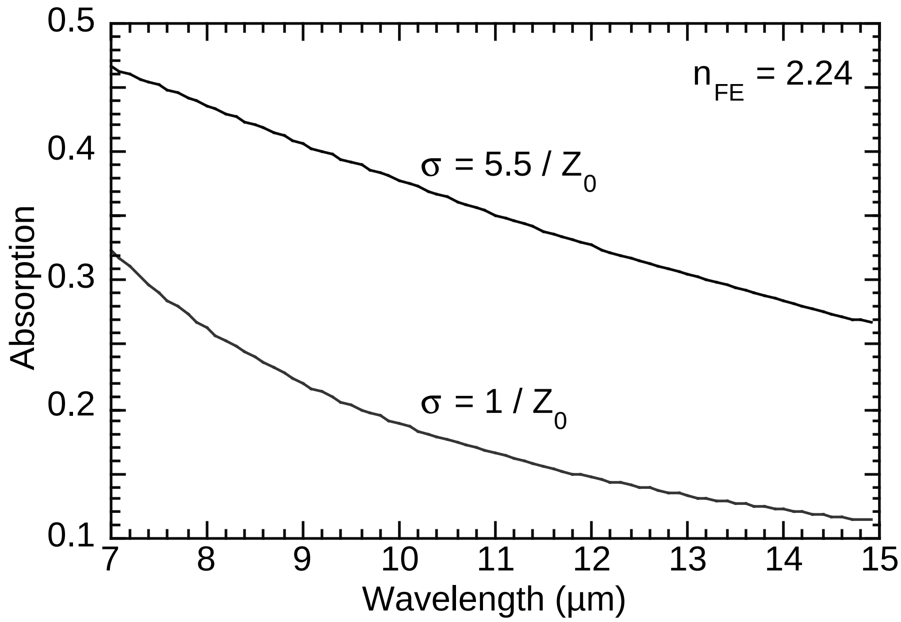

Figure 19: Absorption spectrum for a 3000 Å thick FE structure with opaque back electrode and front electrode with σ = 1/Z_0 and 5.5 / Z_0.

Front and Back Semitransparent Electrodes

The desired detector structure has semitransparent front *and* back electrodes. It is possible to separately optimize the conductivity of each electrode; however, it will generally be desirable to have equal sheet conductivity in both electrodes. Otherwise, the resistance of the less conductive electrode will dominate the electrical resistance and Johnson noise of the detector. Furthermore, as shown below, it is possible to achieve nearly 100 percent absorption (at a single wavelength) in an optimized structure with equal-conductivity electrodes.

For the following figures, we assumed a structure with adjustable cavity spacing and a FE layer with thickness specified between 0 and 5000 Å that was surrounded by equal-conductivity electrodes. For each FE thickness, the electrode conductivity and cavity spacing were varied to achieve maximum absorption at a wavelength of 11 μm. It turned out that an absorption of 100 percent was obtained at all FE thicknesses. The optimum values are shown in Figure 20 for three different values of the FE refractive index. Note that in the limit of FE thickness = 0, the optimum conductivity is 0.5/Z_0 and the optimum cavity thickness is 11 μm/4, which is consistent with a simple λ/4 cavity structure because the two electrodes merge to form a single electrode with conductivity of 1/Z_0.

The corresponding absorption spectra are shown in Figure 21. Note that although all structures achieve 100 percent absorption at 11 μm, the integrated absorption over the LWIR band is somewhat lower for thicker FE layers.

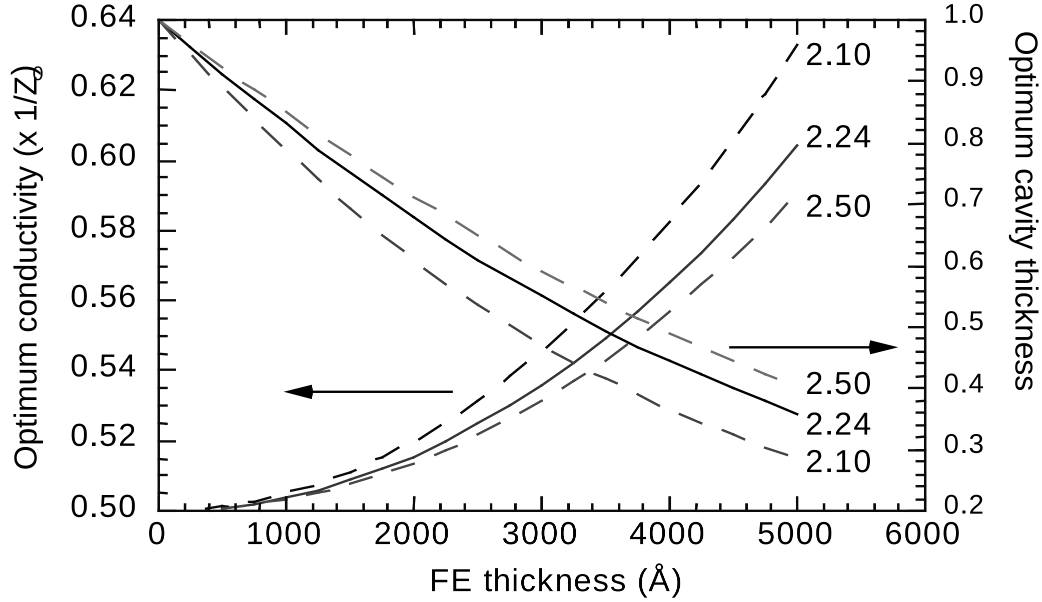

Figure 20: Optimum electrode sheet conductivity ($\times$ 1/Z_0) and cavity thickness vs. FE thickness. Cavity thickness of 1.0 is 11 µm / 4. Refractive index of FE is indicated for each curve.

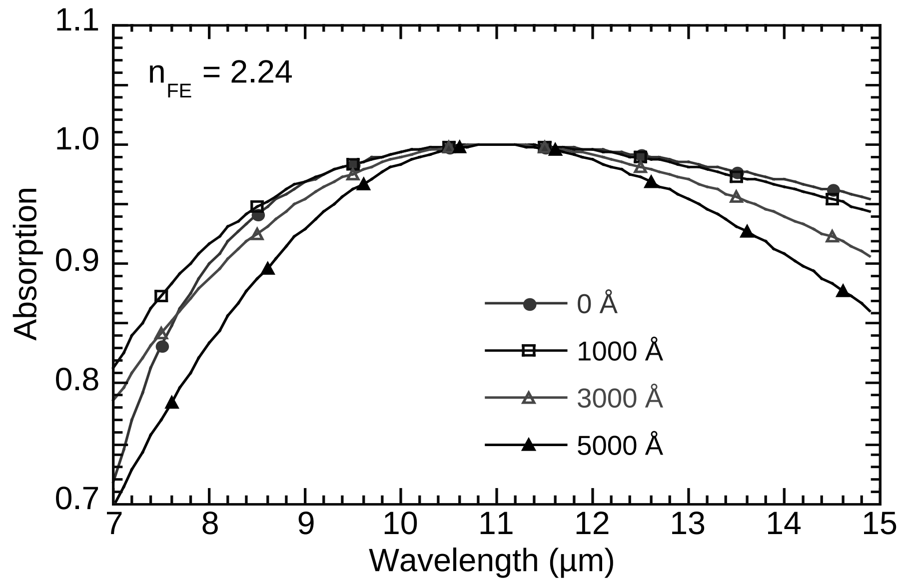

Figure 21: Calculated absorption spectra at several FE thicknesses using optimized parameters from figure 20.

Blackbody Source - *f*/1 Illumination

The results presented so far were for illumination perpendicular to the detector. However, the actual illumination in most uncooled systems would come from a *f*/1 objective. Therefore we computed the absorption for a weighted average over incident angles corresponding to the *f*/1 objective and also averaged over the spectrum of incident power between 8 and 14 µm corresponding to a 300-K blackbody.

The optimum electrode conductivity and cavity thickness were first determined for a structure with equal-conductivity electrodes and a FE layer thickness of 3000 Å. It turned out that the optimum values to achieve maximum integrated absorption ($\sigma = 0.562 / Z_0$, t = 1.594 µm) were only slightly different from the values to achieve maximum normal-incidence absorption at a wavelength of 11 µm ($\sigma = 0.536 / Z_0$, t = 1.507 µm). We then determined the change in total integrated absorption that resulted from deviations from the optimum values. The results, shown in Figure 22, show that it is possible (within the approximations of the present model) to absorb 97.2 percent of LWIR radiation from the *f*/1 objective. Furthermore, the absorption is relatively insensitive to variations in the electrode conductivity and cavity thickness near the optimum point.

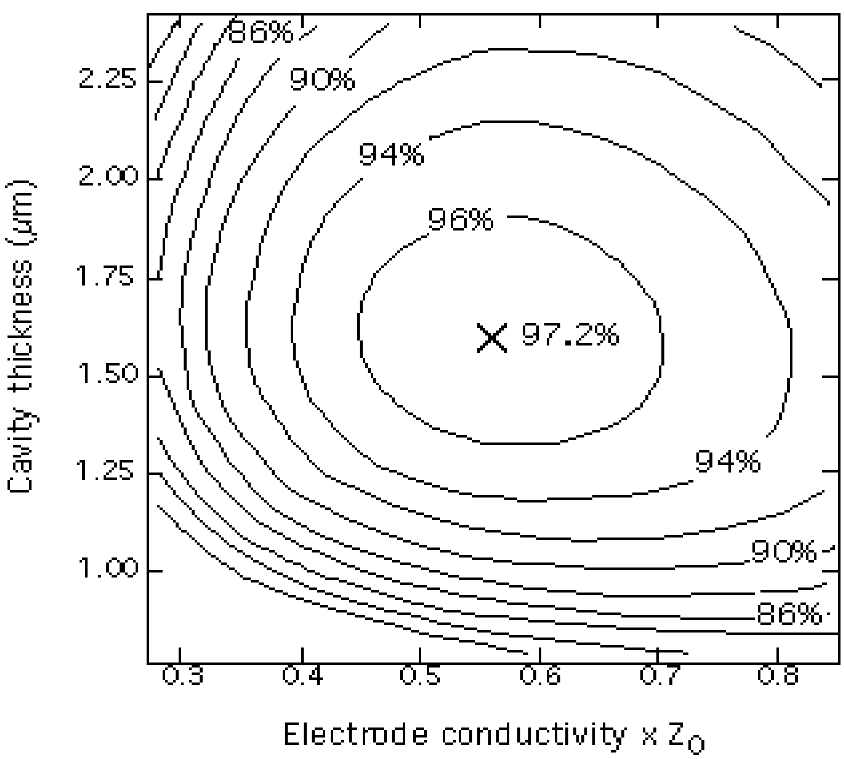

Figure 22: Calculated fraction of incident light absorbed from 300-K blackbody source between 8 and 14 µm. Incident angles simulate a *f*/1 objective. FE layer thickness is 3000 Å.

MODELING OF PIXEL ABSORPTION

Using the Finite Difference Time Domain method (FDTD), one can model the spatial absorption features on an individual pixel. Figure 23 shows the absorption pattern on a pixel for an incident wavelength of 14 µm. It is readily apparent that the absorption is highest at the corners and

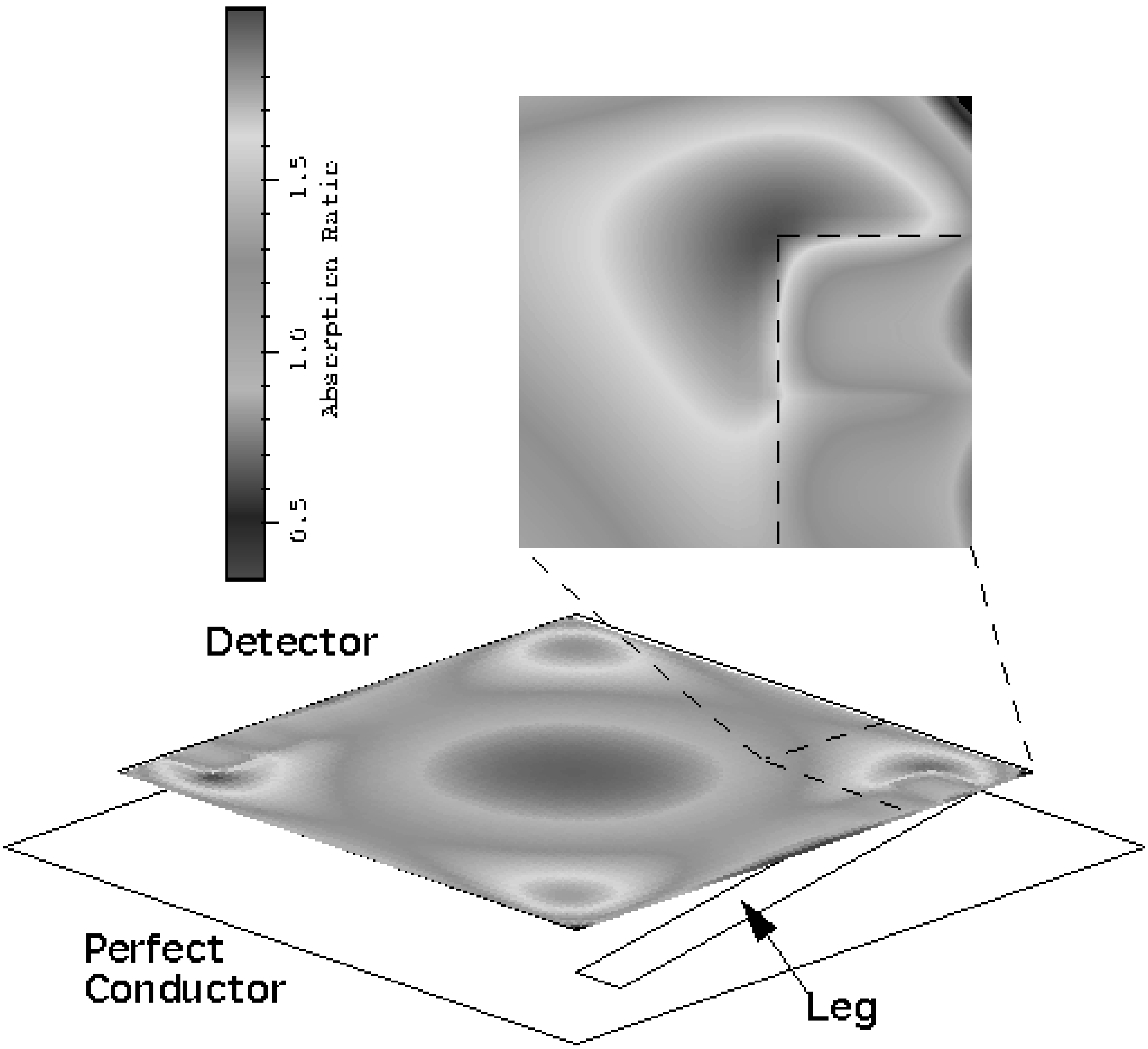

Figure 23: Absorption pattern for unpolarized light with wavelength of 14 µm. Orange is strongest absorption; blue is weakest. Note reduced absorption in center and where legs join detector.

lowest in the center. Also, absorption is reduced at the points where the legs join the pixel. FDTD calculations (see figure 24) also show that there is a slight variation in absorption, depending on whether the incident radiation is polarized parallel or perpendicular to the legs.

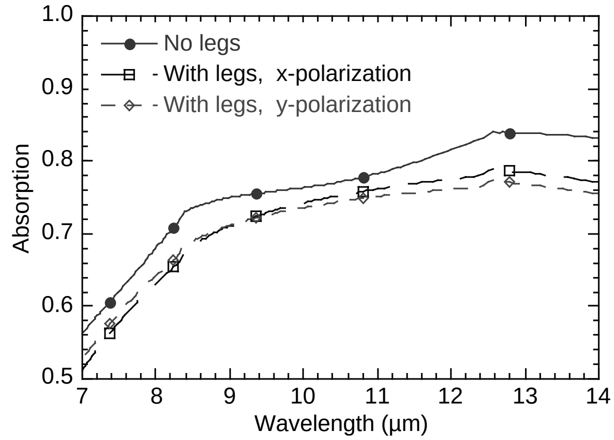

Figure 24: Comparison of absorption with and without legs for 20 µm pixel on 25 µm centers. Absorption with legs depends on polarization of the incident radiation.

CONCLUSIONS

Transmission and reflection measurements indicate that the optical properties of LSCO layers up to 1600-Å thick can be described by a simple two-dimensional conducting sheet whose sheet conductivity increases linearly with film thickness. The bulk resistivity implied by the optical measurements (1.55 mΩ-cm) was comparable to the resistivity determined from four-point probe measurements (1.95 mΩ-cm). These values for as-grown, laser-ablated films are comparable to those previously observed in sputtered LSCO that had been post-growth annealed for 30 to 60 sec at 650 ºC.

A multilayer optical model was used to calculate the expected optical absorption for several important thin-film FE structures, approximating the LSCO semitransparent electrodes as two-dimensional conducting layers. The structure using an opaque back electrode on a 3000-Å-thick ferroelectric is limited to absorption of 20 to 40 percent over the LWIR band.

On the other hand, an optimized structure using equivalent semitransparent front and back electrodes and a vacuum cavity behind the FE layer should have normal-incidence absorption near 100 percent at the design wavelength, and integrated absorption of up to 97 percent of the LWIR power from an *f*/1 objective. The optimum electrode conductivity of 0.5/ Z_0 corresponds to a thickness of around 250 Å for the LSCO films measured for this paper, which is a practical thickness for real detectors.

The conductivities of the RTA annealed films was about half that of the oven-annealed films. Surprisingly, there was only a small difference between the RTA films annealed at 550 °C and those annealed at 600 °C. The conductivities still appear much higher than the optimum value, although in the thinnest LNO films (<250 Å) the conductivity decreases and approaches the optimum value of ~0.5 / Z_0.

Thus, the thinnest LNO films appear to be suitable for device fabrication. This also allows parasitic thermal mass to be minimized. The thinnest film actually measured in this work (450 Å) had an implied sheet conductivity of ~2.5 / Z_0 compared to the optimum value of ~0.5 / Z_0.

The sheet conductance of the BRO films is generally lower than the desired value of of ~(0.5 – 1.0) / Z_0, except for the thickest film. Because the sheet conductances were so low, no attempt was made to plot the values versus thickness.

The sheet conductance of the SRO films covers the desired range quite well at the lower anneal temperatures. For example, with the 400 °C anneal, the 500 and 1000 Å films appear to be close to the desired sheet conductance. Note that the sheet conductance is not proportional to film thickness, i.e., there is an extrapolated finite sheet conductance at zero film thickness. This effect could be associated with an actual surface conductance on the SRO, but is more likely caused by surface roughness that scatters light and thereby shifts the points in the conductivity vs. thickness data. The result is to lower transmission and thus apparently raise conductance. The bulk resistivities implied by the slopes of the linear fits are indicated in the figure.

The characterization of LNO, BRO, and SRO allows greater flexibility in the fabrication of the focal plane array in that it confers to the array designer additional semitransparent electrode materials. This greater selection of electrode materials allows the array designer to select the correct material to achieve the proper electrode conductivity within the stringent thermal budgets needed to fabricate the array.

References

[1] P. Yeh, *Optical Waves in Layered Media* (John Wiley & Sons, New York, 1988).

[2] G. H. Haertling, J. American Ceramic Society **54,** 303-309 (1971).

[3] W. A. Beck, et al., “Infrared Absorption by Ferroelectric Thin Film Structures,” IRIS Materials Group (ERIM, Monterey, 1998)